IEEE Access
Multidisciplinary | Rapid Review | Open Access Journal

Received January 22, 2020, accepted January 28, 2020, date of publication February 3, 2020, date of current version March 3, 2020.

Digital Object Identifier 10.1109/ACCESS.2020.2971019

Single Underwater Image Restoration Based on Adaptive Transmission Fusion

HERNG-HUA CHANG, (Member, IEEE)
Department of Engineering Science and Ocean Engineering, National Taiwan University, Taipei 10617, Taiwan
e-mail: herbertchang@ntu.edu.tw

This work was supported by the Ministry of Science and Technology of Taiwan under Grant MOST 108-2221-E-002-080-MY3.

ABSTRACT Underwater images are often deteriorated with blurring, darkness, poor visual quality of low contrast, and color diminishing. This is mainly due to the fact that the light is exponentially attenuated while traveling through water and the strength of attenuation is color dependent. After constructing a simplified image formation model, this paper proposes a new strategy for single underwater image restoration. In light of different perspectives, two distinct transmission coefficient estimation approaches have been developed. One is based on the optical characteristics while the other relies on the essence of image processing knowledge. Subsequently, these two transmission maps are fused to produce the final outcome, which is adaptively weighted by their respective saliency maps. The obtained signal radiance is dissolved through point spread function deconvolution and color compensation to produce the final scene radiance. A variety of underwater images with various scenarios were exploited to evaluate the restoration performance. Experimental results demonstrated the superiority of the proposed algorithm over other competitive methods for underwater image restoration.

INDEX TERMS Image restoration, transmission fusion, saliency map, dark channel prior, blurriness detection.

I. INTRODUCTION

With rapid advancement in technology the number of underwater images of many kinds has been increased dramatically in recent years. Underwater imaging plays an essential role in a variety of fields such as marine biology, undersea archaeology, mine and wreckage detection, water fauna identification and assessment, and ocean sciences. However, underwater images are often degraded with blurriness, darkness, low contrast, and color diminishing due to particular propagation properties of light absorption and scattering along with unstable environments of water turbidness and light changing [1]. This necessitates the need to either enhance or restore underwater images before further processing and analysis.

The reasons for underwater image degradation can be realized from the characteristics of optics in water. Based on the Beer-Lambert law [2], the absorption comes from an exponential decay term of light attenuation with

$$t(\boldsymbol{x}, \lambda) = e^{-\beta(\lambda) d(\boldsymbol{x})} \tag{1}$$

where $t(\boldsymbol{x}, \lambda)$ is the transmission of light with wavelength λ at scene position $\boldsymbol{x}$, $\beta(\lambda)$ is the spectral volume attenuation coefficient for wavelength λ, and $d(\boldsymbol{x})$ is the distance from the imaging device to the radiant object at $\boldsymbol{x}$. Unlike atmospheric images, the transmission medium is water instead of air, which results in severer deterioration in underwater images. Light attenuation can limit the visibility distance from 20m in clear water down to 5m or less in turbid water [3], [4]. Moreover, red light with its longer wavelength travels the shortest in water and is absorbed more than other colors. As such, the majority of underwater images are exhibited mostly green to blue tones.

One of the pioneering research in underwater optics was proposed by Duntley [5] who defined the fundamental limitations of underwater imaging. Subsequently, McGlamery [6] and Jaffe [7] proposed a notable underwater image formation model called the Jaffe-McGlamery model, which decomposed an underwater image into three major components: direct, forward-scatter, and backscatter components. This model has been the foundation of many studies for the restoration of underwater images. For example, Schechner and Karpel [8] introduced a physics-based scheme

The associate editor coordinating the review of this manuscript and approving it for publication was Qiangqiang Yuan.

to recover visibility while imaging undersea scenes in natural illumination. They observed that the main degradation effects were associated with partial polarization of light. Accordingly, two or more images taken through a polarizer with different orientations were required in their approaches. Nascimento *et al.* [9] proposed an iterative algorithm that was based on classical models of light propagation. Two images taken from an underwater scene under natural illumination were also needed for depth estimation.

While employing multiple images can improve the restoration performance, it requires extra equipment to simultaneously capture the same scene. A more challenging and practical scenario is to perform restoration when only one input image is available. Single underwater image restoration is an ill-posed problem since the amount of scattering, the distance between the scene and the camera, and the light conditions are unknown. Nevertheless, it has drawn much attention in computer vision and image processing. Generally speaking, approaches for single underwater image enhancement and restoration can be broadly divided into two major categories: *image-based* and *model-based*. Image-based methods consider this as a fundamental image processing issue by employing image enhancement techniques without *a priori* assumption. Alternatively, model-based methods tackle this based on different degrees of optical model approximations that generate underwater images.

Examples in the first category include the work by Iqbal *et al.* [10], where the authors introduced a slide stretching scheme to enhance underwater image quality that consisted of two majors steps. Firstly, the contrast stretching was applied to equalize the color image contrast in the RGB (red, green, blue) color space, followed by saturation and stretching in the HSI (hue, saturation, intensity) color model to boost the true color and improve the background lighting. Abdul Ghani and Mat Isa [11] proposed a stretching process in the RGB and HSV (hue, saturation, value) color models for underwater image quality enhancement. They suggested that a better stretching manner for underwater images was to follow the Rayleigh distribution, which effectively eliminated the problems of producing over-dark and over-bright images. The study by Liu and Chau [12] was based on a local contrast enhancement scheme for underwater image restoration. The authors first repeatedly divided the image into four equal rectangular regions until the size was smaller than a specified threshold, from which the waterlight was estimated. Subsequently, a cost function was formulated and minimized to maximize the image contrast. Li *et al.* [13] described a systematic underwater image enhancement framework that was composed of an image dehazing method, which was built on a minimum information loss principle, and a contrast enhancement method, which was based on a histogram distribution assumption.

In contrast to image-based methods, work in the second category made assumptions regarding the formation of underwater images. For example, Trucco and Olmos-Antillon [14] proposed a self-tuning image deconvolution filter based on the Jaffe-McGlamery model. This method automatically estimated the filter parameters in each individual image by optimizing a quality criterion for underwater image restoration. Tarel and Hautiere [15] introduced a linear-time function method for visibility restoration that was capable of handling both color and gray level images. Qiu *et al.* [16] presented a simplified underwater image formation model and developed an adaptive image restoration scheme in light of an improved signal-to-noise ratio. Based on an underwater imaging model, the study by Zhao *et al.* [17] derived inherent optical properties of water from the background color of underwater images for quality enhancement. Liu *et al.* [18] developed a deep sparse non-negative matrix factorization method to estimate the illumination of an underwater image. After the factorization process, the estimated illumination was applied to each patch of the input image to obtain the final output. Cho and Kim [19] described a visibility enhancement algorithm that included an artificial light model in underwater particle physics for visual simultaneous localization and mapping.

Alternatively, Wang *et al.* [20] simplified the full underwater light propagation model and derived a maximum attenuation identification method to estimate the depth map from degraded underwater images. An adaptive attenuation-curve prior was proposed in [21] to restore underwater images. Extended from the concept of the non-local haze-line in [22], this prior estimated the transmission for each pixel according to its distribution on a curve with a power function. Deng *et al.* [23] introduced a removing light source color and dehazing (RLSCD) scheme to perform underwater image enhancement. The scene depth was estimated based on the attenuations of different light conditions and the background light was estimated based on gray open operations. In [24], the authors utilized a multilevel decomposition approach based on L_P-norm decomposition to dissolve an image into three levels: detail, structure, and illuminance. From the original degraded image, two input channels were generated and modulated by their corresponding weight measures. Recently, Cao *et al.* [25] presented the use of a convolutional neural network to estimate background light and a multiscale deep network to determine the transmission map. Liu *et al.* [26] proposed an Underwater Resnet (UResnet) based on the very-deep super-resolution reconstruction (VDSR) model for underwater image enhancement.

Though abundant approaches have been proposed, it is still challenging for underwater image restoration due to the unpredictable variation of vision properties in undersea environments. The ambition of this paper is in an attempt to develop a new underwater image restoration algorithm based on adaptive fusion of image-based and model-based approaches. While taking advantage of both categories, the proposed algorithm strikes a favorable compromise between two kinds of different methods. The main contributions of the current work are summarized as follows:

a) Two different approaches are introduced to compute the background light and integrated into a more accurate estimation.
b) Two transmission maps are computed from distinct perspectives and fused into one single transmission map weighted by their saliency maps.
c) Essential characteristics of model-based and image-based approaches are illustrated and discussed.
d) Influences of the unpredictable variation of undersea vision properties are alleviated due to the proposed fusion scheme for better restoration.
e) Extensive experiments in fair comparison with the state-of-the-art methods are conducted to evaluate the restoration performance.

The remainder of this paper is organized as follows: In Section 2, we deliver a brief review of single underwater image restoration related work. We then describe the proposed methodology in Section 3. The experimental results are presented and discussed in Section 4. Finally, the conclusion is drawn in Section 5.

II. RELATED WORK

A. IMAGE FORMATION MODEL

One simplified and well known underwater image formation model is given as:

$$I(\boldsymbol{x}, \lambda) = J(\boldsymbol{x}, \lambda)\, t(\boldsymbol{x},\lambda) + B(\lambda)\,(1 - t(\boldsymbol{x},\lambda)) \tag{2}$$

where $I(\boldsymbol{x}, \lambda)$ is the observed image perceived from the camera, $J(\boldsymbol{x},\lambda)$ is the scene radiance of the intact image, $t(\boldsymbol{x}, \lambda)$ is the medium transmission coefficient along the ray that describes the portion of the light not backward scattered and reaching the camera as given in (1), and $B(\lambda)$ is the background light. The first term $J(\boldsymbol{x}, \lambda)\, t(\boldsymbol{x}, \lambda)$ on the right-hand side of (2) is treated as direct attenuation and the second term $B(\lambda)(1 - t(\boldsymbol{x}, \lambda))$ indicates *waterlight* illumination. Given $I(\boldsymbol{x}, \lambda)$ and based on (2), the single underwater image restoration problem is to solve $J(\boldsymbol{x}, \lambda)$ by computing $t(\boldsymbol{x}, \lambda)$ and $B(\lambda)$. However, the challenge is how to correctly obtain these two terms using only one single image. Consequently, in this scenario the key to successful restoration of underwater images is a reliable and adequate approximation of the transmission coefficient map and the background light.

B. DARK CHANNEL PRIOR BASED APPROACHES

One famous model-based haze removal algorithm has been the dark channel prior (DCP) scheme proposed by He *et al.* [27] according to (2). The main idea underlining this approach was based on an experimental observation that most local patches in outdoor haze-free images contain pixels whose intensity is fairly low in at least one RGB color channel. To formally describe this observation, the authors defined the dark channel using

$$J^D(\boldsymbol{x}) = \min_{\boldsymbol{y}\in\Omega(\boldsymbol{x})} \left(\min_{\lambda\in\{R,G,B\}} (J(\boldsymbol{y}, \lambda)) \right) \tag{3}$$

where $J^D(\boldsymbol{x})$ is the dark channel of $J(\boldsymbol{x}, \lambda)$, $\Omega(\boldsymbol{x})$ indicates the local patch centered at $\boldsymbol{x}$, and $\lambda \in \{R, G, B\}$ represents the color channel index. Obviously, the dark channel obtains the outcome using two minimum operators: $\min_{\lambda\in\{R,G,B\}}$ finds the minimum value among the three color channels on each pixel, and $\min_{\boldsymbol{y}\in\Omega(\boldsymbol{x})}$ is basically a minimum filer centered at $\boldsymbol{x}$. If $J(\boldsymbol{x}, \lambda)$ is an outdoor haze-free image, $I(\boldsymbol{x},\lambda) = J(\boldsymbol{x}, \lambda)$ and the intensity of $J^D(\boldsymbol{x})$ is pretty low and tends to be zero:

$$J^D(\boldsymbol{x}) \to 0 \tag{4}$$

This observation is called the DCP.

Based on this DCP, the authors efficiently estimated haze thicknesses and adequately recovered haze images. This brilliant framework has become the foundation of many subsequent studies. For example, Li *et al.* [28] described a single image haze removal algorithm by introducing a minimal color channel, through which a simplified dark channel was computed. To accommodate the transmission map, an adaptive sky region compensation term was introduced to avoid amplifying noise in the sky realm. The principal component analysis and minimum volume ellipsoid approximation were utilized by Gibson and Nguyen [29] to explain the effectiveness of the DCP. Based on the approximation of an RGB cluster with the minimum volume ellipsoid, the authors showed the effectiveness of this ellipsoid to geometrically interpret how the DCP works well in hazy images. A fast depth map approximation method using the DCP was presented by Han and Wan [30] for single image dehazing. The approximation made use of the pixel-wise depth map and the observation that most artifacts appeared in the region where the original estimated depth map had large differences from its pixel-wise depth map.

Conceived from the concept of the DCP, a number of approaches for underwater image enhancement and restoration using a single image have been proposed. For example, Chiang and Chen [31] described an underwater image enhancement framework that combined an image dehazing algorithm with a wavelength compensation. The influence of the haze was reduced by modifying the classical DCP algorithm. According to the amount of attenuation corresponding to each light wavelength, the authors administered color change compensation to restore color balance. A two-phase regularization mechanism was proposed by Guo *et al.* [32] to restore underwater image vision. A modified DCP method was developed to remove haze in underwater images followed by a series of color balancing and contrast stretching techniques for making the image color more natural. In spirit similar to the DCP, Galdran *et al.* [33] presented a red channel scheme to rectify underwater image color with short wavelengths, which resulted in luminous contrast enhancement and realistic color correction. The work by Drews *et al.* [34] introduced an underwater DCP that considered only the green and blue channels to restore visual quality of underwater images. Borkar and Bonde [35] extended the DCP to remove

the haze in underwater images using the red channel of a single input underwater image, whose depth map was computed using morphological operations.

C. OTHER APPROACHES WITH IMAGE PROCESSING KNOWLEDGE

There are single image restoration approaches that took advantage of image processing knowledge in facilitating the recovery procedure. Without using any prior, Li and Zheng [36] introduced an edge-preserving decomposition-based method for single image haze removal. A weighted guided image filter was adopted to generate a base layer image, which was further utilized to restore the hazy image. Hou *et al.* [37] applied wavelet decompositions to underwater images for isolating noise from signals. Subsequently, the authors employed the point spread function in the spatial domain and the modulation transfer function in the frequency domain for restoration. Tian and Narasimhan [38] built a compact spatial distortion model of the water surface with the wave equation. Based on this model, they presented a tracking technique while recovering the planar underwater scene without using any image prior. Li *et al.* [39] utilized a quad-tree subdivision and graph-based segmentation scheme for estimating the global background light. The transmission map was then computed using the minimum information loss principle associated with optical properties of underwater imaging.

Recently, Peng and Cosman [40] investigated a single image oriented algorithm to restore underwater images based on image blurriness and light absorption. Better restoration results were obtained in comparison to image formation model-based methods. In their approach, the authors first define the initial blurriness map P_i as

$$P_i(\boldsymbol{x}) = \frac{1}{n}\sum_{i=1}^{n}\left|I_g(\boldsymbol{x}) - G^{r_i,r_i}(\boldsymbol{x})\right| \tag{5}$$

where $I_g(\boldsymbol{x})$ is the grayscale version of $I(\boldsymbol{x}, \lambda)$ in (2), $G^{r_i,r_i}(\boldsymbol{x})$ is the outcome of the input image smoothed by an $r_i \times r_i$ spatial Gaussian filter with standard deviation r_i, where $r_i = 2^i n + 1$ with $n = 4$. The maximum filter was then applied to obtain the rough blurriness map P_r using

$$P_r(\boldsymbol{x}) = \max_{\boldsymbol{y}\in\Omega(\boldsymbol{x})} P_i(\boldsymbol{y}) \tag{6}$$

where $\Omega(\boldsymbol{x})$ is a 7×7 local patch centered at $\boldsymbol{x}$. A refined blurriness map P_b was finally computed with

$$P_b(\boldsymbol{x}) = F_g\left\{C_r[P_r(\boldsymbol{x})]\right\} \tag{7}$$

where C_r is a hole-filling morphological reconstruction operator and F_g is the guided filtering function [41].

To estimate the distance function $d(\boldsymbol{x})$ in (1), the authors proposed three different methods. The first approach is based on the image blurriness $P_r(\boldsymbol{x})$ in (6) through a regulation process using

$$d_1(\boldsymbol{x}) = 1 - \frac{C_r[P_r(\boldsymbol{x})] - \min\left\{C_r[P_r(\boldsymbol{x})]\right\}}{\max\left\{C_r[P_r(\boldsymbol{x})]\right\} - \min\left\{C_r[P_r(\boldsymbol{x})]\right\}} \tag{8}$$

The second estimation for $d(\boldsymbol{x})$ is derived from a disparity map $D(\boldsymbol{x})$ with

$$d_2(\boldsymbol{x}) = 1 - \frac{D(\boldsymbol{x}) - \min\left\{D(\boldsymbol{x})\right\}}{\max\left\{D(\boldsymbol{x})\right\} - \min\left\{D(\boldsymbol{x})\right\}} \tag{9}$$

Herein, it is assumed that a greater value of the disparity indicates the closer the point is to the camera. Similarly, a scene point with more red light is assumed closer to the camera, which gives rise to the third distance estimation

$$d_3(\boldsymbol{x}) = 1 - \frac{R(\boldsymbol{x}) - \min\left\{R(\boldsymbol{x})\right\}}{\max\left\{R(\boldsymbol{x})\right\} - \min\left\{R(\boldsymbol{x})\right\}} \tag{10}$$

where $R(\boldsymbol{x})$ is the red channel map defined as

$$R(\boldsymbol{x}) = \max_{\boldsymbol{y}\in\Omega(\boldsymbol{x})} I(\boldsymbol{y}, R) \tag{11}$$

These three distance functions are then consolidated to form a single distance estimation $d_s(\boldsymbol{x})$ using

$$d_s(\boldsymbol{x}) = \eta_1\left[\eta_2 d_2(\boldsymbol{x}) + (1-\eta_2)\, d_3(\boldsymbol{x})\right] + (1-\eta_1) d_1(\boldsymbol{x}) \tag{12}$$

where

$$\eta_1 = S\left(\text{mean}\left(I(\boldsymbol{x}, R)\right), 0.1\right) \tag{13}$$

and

$$\eta_2 = S\left(\text{mean}\left(B(\lambda)\right), 0.5\right) \tag{14}$$

with S the sigmoid function.

III. PROPOSED METHODS

A. OPTICAL MODEL

Figure 1 illustrates the proposed optical model for underwater image formation. The perceived image captured by the camera consists of three major components with

$$I(\boldsymbol{x}, \lambda) = E_d(\boldsymbol{x}, \lambda) + E_f(\boldsymbol{x}, \lambda) + E_b(\boldsymbol{x}, \lambda) \tag{15}$$

where $E_d(\boldsymbol{x}, \lambda)$ is the direct component, $E_f(\boldsymbol{x}, \lambda)$ is the forward scattered component, and $E_b(\boldsymbol{x}, \lambda)$ is the backscattered

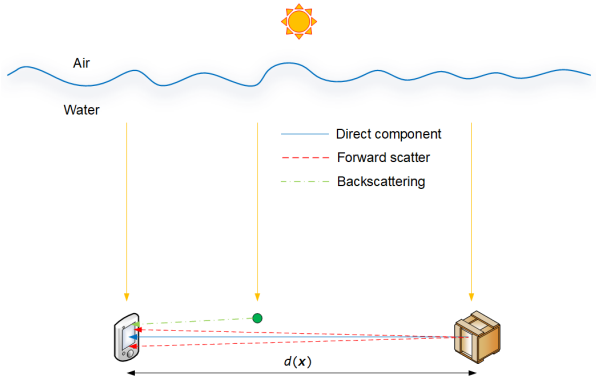

FIGURE 1. The proposed underwater imaging model with simplified optical characteristics.

component. The direct irradiance is related to the characteristics of the medium through exponentially decayed dependence as

$$E_d(\boldsymbol{x}, \lambda) = E_v(\lambda)\, e^{-\beta(\lambda) d(\boldsymbol{x})} \tag{16}$$

where $E_v(\lambda)$ is the radiance of the object due to vertical absorption. The other light reflected by the object but scattered at a small angle constitutes the forward scattered component that is modeled as

$$E_f(\boldsymbol{x}, \lambda) = E_d(\boldsymbol{x}, \lambda) * g(\boldsymbol{x}, \lambda) \tag{17}$$

where the operator $*$ represents convolution and $g(\boldsymbol{x}, \lambda)$ is the point spread function. The backscattered component results from the interaction between the illumination source and the floating particles dispersed in the water, which is estimated using

$$E_b(\boldsymbol{x}, \lambda) = B(\lambda)\left(1 - e^{-\beta(\lambda) d(\boldsymbol{x})}\right) \tag{18}$$

From the viewpoint of optics, the direct and forward scattered components comprise the signal because they all originate from the object. Accordingly, we define the signal irradiance $E_s(\boldsymbol{x}, \lambda)$ as

$$\begin{aligned} E_s(\boldsymbol{x}, \lambda) &= E_d(\boldsymbol{x}, \lambda) + E_f(\boldsymbol{x}, \lambda) \\ &= E_v(\lambda)\, e^{-\beta(\lambda) d(\boldsymbol{x})} + E_v(\lambda)\, e^{-\beta(\lambda) d(\boldsymbol{x})} * g(\boldsymbol{x}, \lambda) \\ &= E_v(\lambda)\, e^{-\beta(\lambda) d(\boldsymbol{x})} * [\delta(\boldsymbol{x}) + g(\boldsymbol{x}, \lambda)] \\ &= E_d(\boldsymbol{x}, \lambda) * [\delta(\boldsymbol{x}) + g(\boldsymbol{x}, \lambda)] \end{aligned} \tag{19}$$

where $\delta(\boldsymbol{x})$ represents the Dirac delta function. Substitute (18) and (19) into (15), we can rewrite $I(\boldsymbol{x}, \lambda)$ as

$$I(\boldsymbol{x}, \lambda) = E_s(\boldsymbol{x}, \lambda) + B(\lambda)\left(1 - e^{-\beta(\lambda) d(\boldsymbol{x})}\right) \tag{20}$$

Substitute (1) into (20), we can express $I(\boldsymbol{x}, \lambda)$ in terms of the $E_s(\boldsymbol{x}, \lambda)$, $B(\lambda)$, and $t(\boldsymbol{x}, \lambda)$ using

$$I(\boldsymbol{x}, \lambda) = E_s(\boldsymbol{x}, \lambda) + B(\lambda)(1 - t(\boldsymbol{x}, \lambda)) \tag{21}$$

Similar to (2), our task now is to compute the background light and the transmission coefficient for solving the signal irradiance given a single underwater image $I(\boldsymbol{x}, \lambda)$. Two approaches derived from different perspectives are proposed and integrated into one final solution for each computation.

B. BACKGROUND LIGHT ESTIMATION

Our first background light estimation comes from the observation of the characteristics in undersea environments. In most underwater images, the dominating color due to light diminishing and/or the presence of planktonic algae is green to blue. Aa such, we define a disparity map $D(\boldsymbol{x})$ as

$$D(\boldsymbol{x}) = I(\boldsymbol{x}, R) - \max(I(\boldsymbol{x}, G), I(\boldsymbol{x}, B)) \tag{22}$$

where $D(\boldsymbol{x})$ is the intensity difference between the red channel component $I(\boldsymbol{x}, R)$ and the maximum of the green channel $I(\boldsymbol{x}, G)$ and the blue channel $I(\boldsymbol{x}, B)$ components. The first background light $B_1(\lambda)$ is estimated by averaging the intensity values at locations that have the most significant disparity based on $D(\boldsymbol{x})$ using

$$B_1(\lambda) = \text{mean}\left(I\left(\hat{\boldsymbol{x}}_1, \lambda\right)\right) \tag{23}$$

where $\hat{\boldsymbol{x}}_1$ is the set of positions that possess absolute $D\left(\hat{\boldsymbol{x}}_1\right)$ magnitudes within the preceding ξ_1 percent.

Stimulated by the blurriness computation in [40], we locate the background light candidate positions of the second group according to (7) with

$$B_2(\lambda) = \text{mean}\left(I\left(\hat{\boldsymbol{x}}_2, \lambda\right)\right) \tag{24}$$

where $\hat{\boldsymbol{x}}_2$ is the locations where their absolute $P_b\left(\hat{\boldsymbol{x}}_2\right)$ magnitudes are within the preceding ξ_2 percent. The final background light is obtained by integrating both estimations using

$$B(\lambda) = \alpha(\lambda) B_{\max}(\lambda) + (1 - \alpha(\lambda)) B_{\min}(\lambda) \tag{25}$$

where

$$B_{\max}(\lambda) = \max(B_1(\lambda), B_2(\lambda)) \tag{26}$$

$$B_{\min}(\lambda) = \min(B_1(\lambda), B_2(\lambda)) \tag{27}$$

and the weight $\alpha(\lambda)$ is computed through a sigmoid function

$$\alpha(\lambda) = S(\psi(\lambda), p) = [1 + e^{-s(\psi(\lambda) - p)}]^{-1} \tag{28}$$

where $p = 0.2$ is a shape factor, $s = 32$ is an empirical constant, and $\psi(\lambda)$ is related to the lighting conditions of the input image with

$$\psi(\lambda) = \frac{|I(\boldsymbol{x}, \lambda) > I_\epsilon|}{MN} \tag{29}$$

where I_ϵ is an intensity threshold for counting the number of pixels brighter than this value (e.g., half of the maximum possible intensity) in the numerator, and M and N are the width and length of the input image, respectively.

Figure 2 illustrates the effectiveness of the proposed background light integration scheme, where the input underwater image is severely blurred and distorted. While the restoration using B_1 in (23) is dark with greenish artefact, the restored image by B_2 in (24) is somewhat too saturated to reveal the far distant details. It is demonstrated that the integrated background light based on (25) strikes a good compromise between brightness and contrast. On the other hand, the restoration outcome based on [40] is still greenish with some blurriness. The background light estimation in [40] requires the iterative decomposition of the input image according to the variance or blurriness using a quadtree scheme. As such, the background light is estimated in square regions, which may exclude some important background light areas. When there are many similar regions in the input image, the estimated background light could be misleading. Moreover, the background light estimation procedure in [40] is more time consuming with 115 ms comparing to 57 ms using the proposed strategy in the restoration illustration of Fig. 2.

FIGURE 2. Illustration of the effectiveness of the background light estimation procedure, where B_1, B_2, and B are computed based on (23), (24), and (25), respectively.

C. TRANSMISSION COEFFICIENT ESTIMATION BY DCP-W

Inspired by the DCP, we previously proposed a new dark channel prior-water (DCP-W) for a haze-free underwater image [42]. By introducing the DCP-W, normalizing (21) with $B(\lambda)$, and applying the minimum operators, we can obtain the following formula:

$$\max_{\lambda\in\{R,G,B\}}\left(\tilde{t}\left(\boldsymbol{x},\lambda\right)\right) = 1-\min\left(\frac{\min\limits_{\boldsymbol{y}\in\Omega(\boldsymbol{x})}\left(1-I\left(\boldsymbol{y},R\right)\right)}{B\left(R\right)},\frac{\min\limits_{\boldsymbol{y}\in\Omega(\boldsymbol{x})}\left(I\left(\boldsymbol{y},G\right)\right)}{B\left(G\right)},\frac{\min\limits_{\boldsymbol{y}\in\Omega(\boldsymbol{x})}\left(I\left(\boldsymbol{y},B\right)\right)}{B\left(B\right)}\right) \tag{30}$$

where $\tilde{t}\left(\boldsymbol{x},\lambda\right)$ is the transmission coefficient map under the constant local patch ($\Omega\left(\boldsymbol{x}\right)$) assumption. Since the blue attenuation coefficient is the weakest among the three colors, the transmission coefficient of the blue channel dominates the left-hand side of (30). The estimated blue transmission map of our first perspective can be computed using [42]

$$\tilde{t}_1\left(\boldsymbol{x},B\right) = 1-\min\left(\frac{\min\limits_{\boldsymbol{y}\in\Omega(\boldsymbol{x})}\left(1-I\left(\boldsymbol{y},R\right)\right)}{B\left(R\right)},\frac{\min\limits_{\boldsymbol{y}\in\Omega(\boldsymbol{x})}\left(I\left(\boldsymbol{y},G\right)\right)}{B\left(G\right)},\frac{\min\limits_{\boldsymbol{y}\in\Omega(\boldsymbol{x})}\left(I\left(\boldsymbol{y},B\right)\right)}{B\left(B\right)}\right) \tag{31}$$

The transmission coefficient maps of the green and red channels are estimated respectively using [42]

$$\tilde{t}_1\left(\boldsymbol{x},G\right) = \left(e^{-\beta(B)d(\boldsymbol{x})}\right)^{\frac{\beta(G)}{\beta(B)}} = \tilde{t}_1\left(\boldsymbol{x},B\right)^{\frac{\beta(G)}{\beta(B)}} \tag{32}$$

and

$$\tilde{t}_1\left(\boldsymbol{x},R\right) = \left(e^{-\beta(B)d(\boldsymbol{x})}\right)^{\frac{\beta(R)}{\beta(B)}} = \tilde{t}_1\left(\boldsymbol{x},B\right)^{\frac{\beta(R)}{\beta(B)}}. \tag{33}$$

D. TRANSMISSION COMPUTATION BY DISTANCE ESTIMATION

Our second transmission computation originates from the perspective of the distance function in (1). Conceived from [40], the distance d_0 between the camera and the nearest scene point is estimated using

$$d_0 = 1-\max_{\boldsymbol{x},\lambda}\left\{\frac{\left|B\left(\lambda\right)-I\left(\boldsymbol{x},\lambda\right)\right|}{\max\left[B\left(\lambda^*\right),1-B\left(\lambda^*\right)\right]}\right\} \tag{34}$$

where $\lambda^* = \text{argmax}_{\lambda\in\{R,G,B\}}\left[\max_{\boldsymbol{x}}\left|B\left(\lambda\right)-I\left(\boldsymbol{x},\lambda\right)\right|\right]$ and $d_0 \in [0,1]$. Combining (12) and (34), the final distance function is estimated as

$$d_f\left(\boldsymbol{x}\right) = \Phi\times\left(d_s\left(\boldsymbol{x}\right)+d_0\right) \tag{35}$$

where Φ is a scaling constant for converting the normalized distance to the physical distance. The transmission map of the red channel based on $d_f\left(\boldsymbol{x}\right)$ is computed with [40]

$$\tilde{t}_2\left(\boldsymbol{x},R\right) = e^{-\beta(R)d_f(\boldsymbol{x})} \tag{36}$$

The other two transmission maps can be similarly obtained using [40]

$$\tilde{t}_2\left(\boldsymbol{x},G\right) = \left(e^{-\beta(R)d_f(\boldsymbol{x})}\right)^{\frac{\beta(G)}{\beta(R)}} = \tilde{t}_2\left(\boldsymbol{x},R\right)^{\frac{\beta(G)}{\beta(R)}} \tag{37}$$

and

$$\tilde{t}_2\left(\boldsymbol{x},B\right) = \left(e^{-\beta(R)d_f(\boldsymbol{x})}\right)^{\frac{\beta(B)}{\beta(R)}} = \tilde{t}_2\left(\boldsymbol{x},R\right)^{\frac{\beta(B)}{\beta(R)}}. \tag{38}$$

E. TRANSMISSION FUSION AND SIGNAL RECOVERY

Image fusion is a pragmatic procedure that aims at the creation of a single composite image from multiple input images, which is known as synergy [43]. It is defined as the process of integrating relevant information from two (or more) images of the same scene into a single output image, which is more informative for human visual perception or for computer processing [44]. Studies of existing image fusion methods along with their applications suggest that the output image from the fusion process can provide us with an improved quality than the one provided by any of the individual input images [45]. More specifically, the benefits of image fusion include reduced uncertainty, increased reliability, extended spatial and temporal coverage, and compact representation of information [43]. As such, one primary objective of fusing transmission maps is to mitigate the influence of the unpredictable variation of vision properties in underwater environments. Image fusion can be broadly classified into three classes: pixel-level, feature-level, and decision-level. Artifact free and pattern conservation are the two major requirements for a good image fusion algorithm [46]. The pixel-level image

fusion approach appears to be a natural choice for visualization applications as in our scenario.

To eliminate potential artefacts and speckles in the estimated transmission maps while maintaining scene details during the fusion process, a saliency procedure is performed in advance using

$$\tilde{t}_i^s(\boldsymbol{x},\lambda) = \left\| \mathcal{B}\left[\tilde{t}_i(\boldsymbol{x},\lambda)\right] - \text{mean}\left[\tilde{t}_i(\boldsymbol{x},\lambda)\right] \right\| \tag{39}$$

where $\mathcal{B}$ represents the bilateral filter operator [47] and $\tilde{t}_i^s(\boldsymbol{x},\lambda)$ is the transmission saliency map with $i = 1, 2$. The two transmission maps are then fused into one single transmission map $\tilde{t}(\boldsymbol{x},\lambda)$ using [48]

$$\tilde{t}(\boldsymbol{x},\lambda) = \sum_{i=1}^{2} w_i(\boldsymbol{x},\lambda)\,\tilde{t}_i(\boldsymbol{x},\lambda) \tag{40}$$

where $w_i(\boldsymbol{x},\lambda)$ is the weight based on the transmission saliency map with

$$w_i(\boldsymbol{x},\lambda) = \frac{\tilde{t}_i^s(\boldsymbol{x},\lambda)}{\sum_{j=1}^{2}\tilde{t}_j^s(\boldsymbol{x},\lambda)} \tag{41}$$

where $\sum_{i=1}^{2} w_i(\boldsymbol{x},\lambda) = 1$. The obtained transmission map is further refined using the guided filter [41] and denoted as $\hat{t}(\boldsymbol{x},\lambda)$. Substitute $\hat{t}(\boldsymbol{x},\lambda)$ into (14) and set a lower bound t_0 to the transmission coefficient, we can recover the signal radiance using

$$E_s(\boldsymbol{x},\lambda) = I(\boldsymbol{x},\lambda) - B(\lambda)\left(1 - \max\left(\hat{t}(\boldsymbol{x},\lambda), t_0\right)\right). \tag{42}$$

Figure 3 illustrates the effectiveness of the proposed transmission fusion procedure with respect to the recovered signal radiance E_s. The first transmission map $\tilde{t}_1$ is rugged with speckles so that the recovered E_s is generally dark with green spots. In contrast to $\tilde{t}_1$, the second transmission map is overall more uniform and brighter without showing the proper scene depth. Consequently, the recovered radiance is still greenish and similar to the input image. It is demonstrated that the transmission fusion map $\tilde{t}$ takes advantage of both transmission maps in that the fine details are revealed with proper depth information. Accordingly, the recovered E_s by $\tilde{t}$ exhibits better contrast and vivider color than $\tilde{t}_1$ and $\tilde{t}_2$.

F. SCENE RADIANCE RECOVERY

Since $E_s(\boldsymbol{x},\lambda)$ comprises $E_d(\boldsymbol{x},\lambda)$ and $E_f(\boldsymbol{x},\lambda)$, it is crucial to remove the forward scattered effect from $E_s(\boldsymbol{x},\lambda)$ to obtain $E_d(\boldsymbol{x},\lambda)$. In our approach, the point spread function $g(\boldsymbol{x},\lambda)$ in (17) is modeled as [7]

$$g(\boldsymbol{x},\lambda) = \left(e^{-Ad(\boldsymbol{x})} - e^{-\beta(\lambda)d(\boldsymbol{x})}\right)\Im^{-1}\left\{e^{-Bd(\boldsymbol{x})f}\right\} \tag{43}$$

where A and B are empirical constants, $\Im^{-1}$ is the inverse Fourier transform, and f is the radial frequency. Substitute (43) into (19) and take the Fourier transform on both sides, we obtain

$$\Im\{E_s(\boldsymbol{x},\lambda)\} = \Im\{E_d(\boldsymbol{x},\lambda)\} \times \left\{1 + \Im\left[e^{-Ad(\boldsymbol{x})} - e^{-\beta(\lambda)d(\boldsymbol{x})}\right]e^{-Bd(\boldsymbol{x})f}\right\} \tag{44}$$

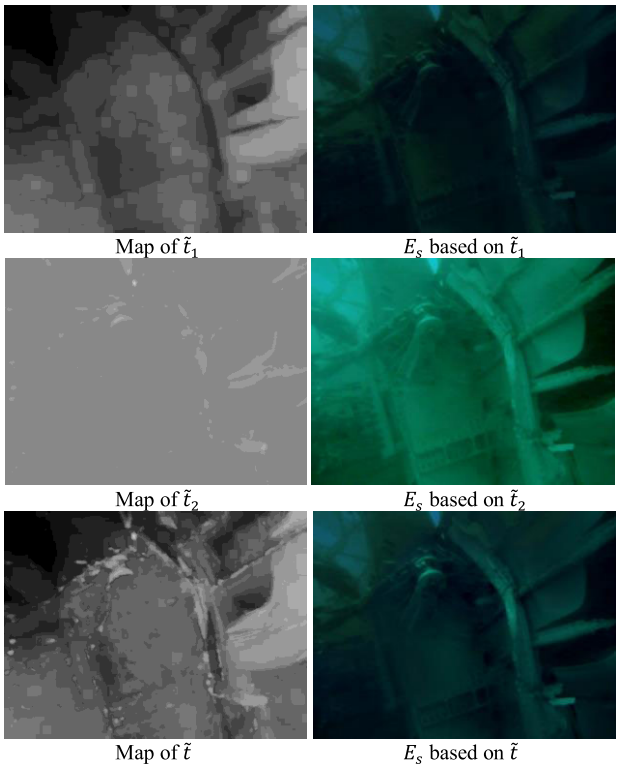

FIGURE 3. Illustration of the effectiveness of the transmission fusion procedure using the same input image in Fig. 2.

where $\Im$ is the Fourier transform. Assuming that the inner Fourier transform in the bracket is constant, we have

$$\Im\{E_s(\boldsymbol{x},\lambda)\} = \Im\{E_d(\boldsymbol{x},\lambda)\}\left\{1 + Ke^{-Bd(\boldsymbol{x})f}\right\} \tag{45}$$

where $K = \Im\left[e^{-Ad(\boldsymbol{x})} - e^{-\beta(\lambda)d(\boldsymbol{x})}\right]$. The direct component $E_d(\boldsymbol{x},\lambda)$ is computed with the blind deconvolution method [49] using

$$E_d(\boldsymbol{x},\lambda) = \frac{E_s(\boldsymbol{x},\lambda)}{\Im^{-1}\left\{1 + Ke^{-Bd(\boldsymbol{x})f}\right\}} \tag{46}$$

Subsequently, the vertical radiance $E_v(\lambda)$ is estimated through the transmission coefficient with

$$E_v(\lambda) = \frac{E_d(\boldsymbol{x},\lambda)}{\max\left(\hat{t}(\boldsymbol{x},\lambda), t_0\right)} \tag{47}$$

To compensate color distortion due to vertical attenuation, the ultimate radiance $E_u(\lambda)$ is recovered using a simple color correction as

$$E_u(\lambda) = E_v(\lambda) + (\mu_\lambda - \text{mean}(E_v(\lambda))) \tag{48}$$

where μ_λ is the desired mean intensity for each channel. Finally, in Fig. 4, we depict the flowchart of the proposed single underwater image restoration framework.

IV. EXPERIMENTAL RESULTS

To quantitatively evaluate the restoration performance of the tested methods, several performance measure metrics were

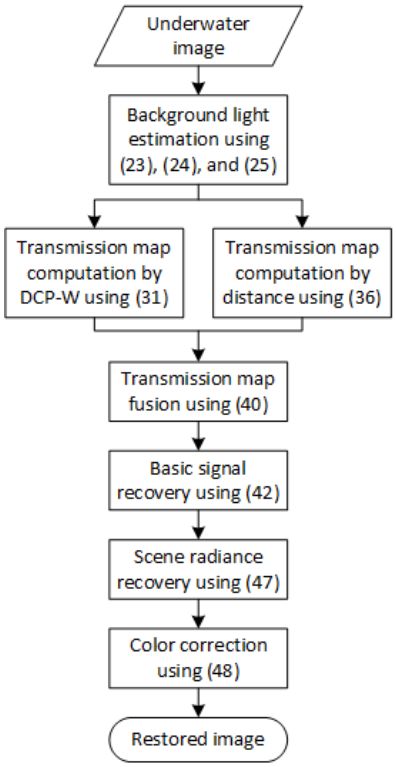

FIGURE 4. Flowchart of the proposed single underwater image restoration framework.

employed. For color correctness assessment, a straightforward pixel-by-pixel channel intensity disparity is defined as

$$\delta = \frac{\sum_{\lambda\in\{R,G,B\}} \left(I_{gt}\left(\boldsymbol{x},\lambda\right) - I_{rt}\left(\boldsymbol{x},\lambda\right)\right)^2}{MN} \tag{49}$$

where δ is the normalized color deviation metric, I_{gt} is the ground truth image, I_{rt} is the restored image, and both images are normalized with the maximum intensity to unity. A smaller value of δ suggests better color correction ability.

To understand the overall restoration performance without the knowledge of the ground truth image, the underwater image quality measure (UIQM) [50] was utilized. The UIQM metric is a linear combination of three independent image quality measures using

$$\text{UIQM} = c_1 \times \text{UICM} + c_2 \times \text{UISM} + c_3 \times \text{UIConM} \tag{50}$$

where UICM is the colorfulness, UISM is the sharpness, and UIConM is the contrast measure. The parameters c_1, c_2, and c_3 are weights, whose values are application dependent. In this paper, we have set the values as follows: $c_1 = 0.3282$, $c_2 = 0.2953$, and $c_3 = 3.5753$. A greater score of the UIQM metric indicates superior image quality.

A. UNDERWATER IMAGE DATABASES

A variety of underwater images with different levels of turbidness and distinct scenarios of distortion were utilized to evaluate the proposed restoration framework, which involve three different databases:

1. AL-NG-OVD Database: This dataset consists of 143 diverse underwater images acquired from the websites of the aqua life (AL) [51], national geographic (NG) [52], and ocean view diving (OVD) 53].
2. Deep-sea debris (D-SD) Database: This dataset comprises 98 marine debris images, which were collected from the public website that is owned by the Japan Agency for Marine-Earth Science and Technology (JAMSTEC) [54].
3. Hawaii Institute of Marine Biology (HIMB) Database: This dataset contains 37 challenging stereo underwater images, which were selected from the coral site images of HIMB#1 dataset [55].

The entire system was implemented and programmed in MATLAB 2018 (The MathWorks Inc. Natick, MA, USA). All experiments were executed on an Intel®Core(TM) i5 CPU @ 2.50GHz with 8 GB RAM running 64-bit Windows 10. Experimental results produced by our algorithm were compared to six state-of-the-art methods of the integrated color model (ICM) [10], enhancement with Rayleigh distribution (ERD) [11], underwater dark channel prior (UDCP) [34], image blurriness and light absorption (IBLA) [40], underwater light scattering model (ULSM) [19], and non-local image dehazing (N-LID) [22].

B. PARAMETER SENSITIVITY

In our implementation, the intensity of the input image was normalized to [0, 1] with double precision before processing. The parameter μ_λ in (48) was automatically computed as the median of the mean intensities of the three channels. To understand the influence of the scaling constant Φ in (35) and the lower bound t_0 in (42), we first investigated the setting of these essential parameters in the restoration process. As illustrated in Fig. 5, there was no significant difference between various settings of the scaling constant. Based on the examples, it was demonstrated that $\Phi = 5$ was a good choice for most situations. For the value of the lower bound, extensive tests suggested $t_0 = 0.3$, which was a favorable comprise between clarity and vagueness as shown in Fig. 5.

C. RESTORATION OF COLOR BOARD IMAGES

We then evaluated the color correction performance on color board images. The ground truth image was distorted and deteriorated based on the Jaffe-McGlamery model [6], [7] to simulate the undersea environments in depths from 1 to 20 m. The underwater color board images beneath the sea level 3M and 9M and their corresponding recovery results were illustrated in Fig. 6. Table 1 presents quantitative analyses of the restoration results using the IBLA, ERD, UDCP, ICM, and proposed methods based on the normalized color deviation metric in (49). Our restoration framework not only produced the smallest δ value in each depth but also achieved the lowest average score ($\bar{\delta} = 0.0087$) among all tested methods.

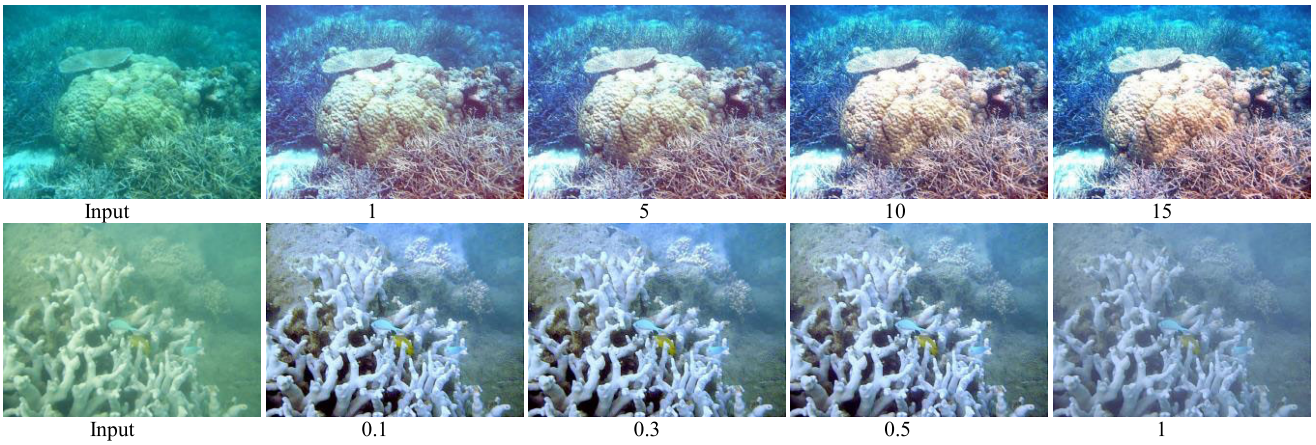

FIGURE 5. Sensitivity analysis of the parameters. Top: the scaling constant Φ in (35). Bottom: the lower bound t_0 in (42).

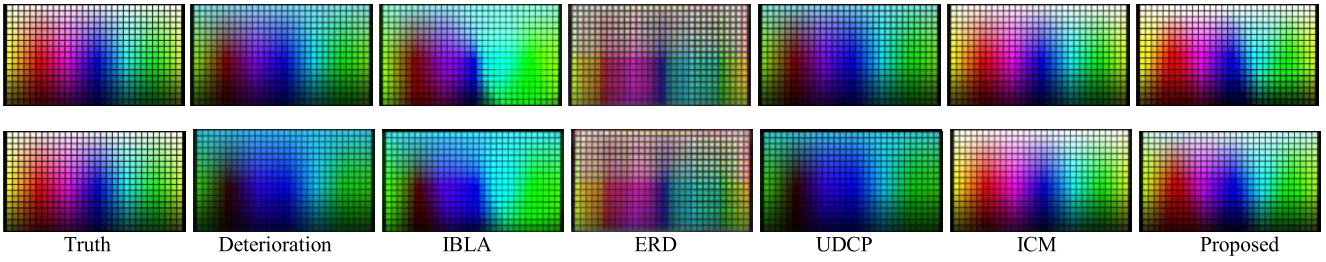

FIGURE 6. Restoration of the deteriorated color board images 3M (top) and 9M (bottom) in depth.

TABLE 1. Restoration evaluation of the color board images in terms of the normalized color deviation metric, δ.

Depth (m)	ICM	ERD	UDCP	IBLA	Proposed
1	0.0058	0.0423	0.0143	0.0291	0.0046
2	0.0084	0.0437	0.0237	0.0369	0.0057
3	0.0101	0.0448	0.0324	0.0440	0.0067
4	0.0114	0.0439	0.0404	0.0502	0.0075
5	0.0122	0.0432	0.0479	0.0600	0.0085
6	0.0127	0.0434	0.0544	0.0645	0.0081
7	0.0129	0.0424	0.0544	0.0681	0.0088
8	0.0133	0.0406	0.0606	0.0667	0.0084
9	0.0132	0.0391	0.0715	0.0693	0.0090
10	0.0138	0.0393	0.0761	0.0715	0.0089
11	0.0137	0.0374	0.0815	0.0746	0.0091
12	0.0133	0.0355	0.0854	0.0778	0.0095
13	0.0133	0.0390	0.0886	0.0801	0.0100
14	0.0139	0.0348	0.0921	0.0831	0.0097
15	0.0137	0.0354	0.0947	0.0857	0.0098
16	0.0135	0.0343	0.0976	0.0885	0.0099
17	0.0133	0.0343	0.0997	0.0910	0.0101
18	0.0129	0.0334	0.1008	0.0924	0.0095
19	0.0128	0.0338	0.1044	0.0942	0.0099
20	0.0128	0.0329	0.1057	0.0963	0.0097
Avg.	0.0124	0.0387	0.0719	0.0712	**0.0087**

D. RESTORATION OF UNDERWATER IMAGES

A number of underwater images were utilized to evaluate the restoration performance of the proposed framework in comparison with the state-of-the-art methods. Fig. 7 depicts the recovery of Scene 1 image in the AL-NG-OVD database along with the UIQM scores. While the restoration results of

TABLE 2. Quantitative performance analyses of different methods based on three underwater image databases using the UIQM metric.

Database	Input	ICM	ERD	UDCP	IBLA	ULSM	N-LID	Proposed
AL-NG-OVD	1.556 ± 1.12	2.519 ± 0.90	2.818 ± 0.77	2.907 ± 0.98	2.573 ± 1.24	2.215 ± 0.94	3.258 ± 1.30	$\mathbf{4.210 \pm 1.27}$
D-SD	1.419 ± 0.40	1.718 ± 0.37	2.174 ± 0.48	2.508 ± 0.63	2.283 ± 0.52	2.098 ± 0.54	2.945 ± 0.74	$\mathbf{3.249 \pm 0.80}$
HIMB	0.612 ± 0.36	1.554 ± 0.37	2.843 ± 0.63	1.989 ± 0.78	1.735 ± 0.92	1.206 ± 0.46	2.105 ± 0.60	$\mathbf{3.746 \pm 1.13}$

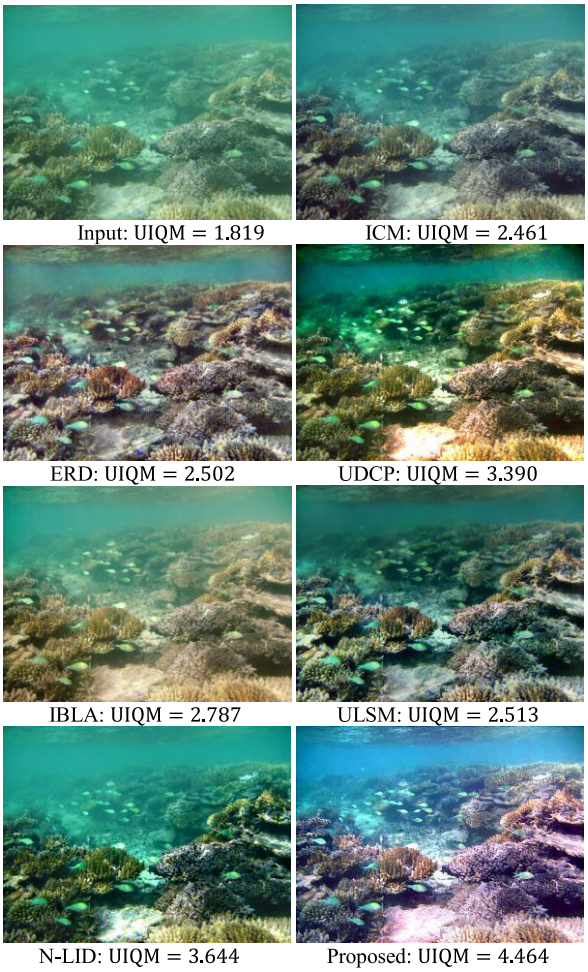

FIGURE 7. Visual comparison of restoration in Scene 1 image.

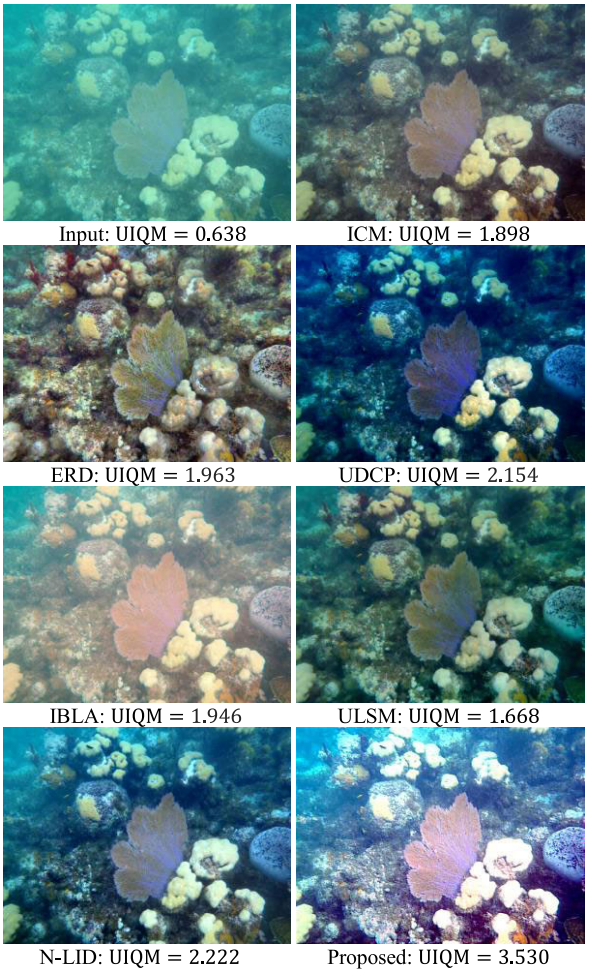

FIGURE 8. Visual comparison of restoration in Scene 2 image.

the ICM, N-LID, and IBLA methods were somewhat greenish, the foreground scenes of the ERD, UDCP, ULSM, and proposed methods were relatively clear. Moreover, the contrast of the foreground using the ERD and UDCP methods was somewhat over-enhanced comparing to our algorithm ($\mu_\lambda = 0.5186$), which produced the largest UIQM score of 4.464. The restoration results of another representative image (Scene 2) with green distortion from the AL-NG-OVD database were shown in Fig. 8. The ICM, ERD, IBLA, and ULSM methods generated somewhat similar color tone outcomes. The UDCP method darkened the image with blue distortion, whereas the results of the N-LID and proposed methods revealed the foreground while maintaining some vagueness in the background.

Figure 9 presents the restoration of Scene 3 image in the AL-NG-OVD database, which is deteriorated by bluish haze. While the background scenes generated by the ERD and ULSM methods were darkish, all other methods more or less maintained the bluish background. Particularly, the proposed restoration scheme ($\mu_\lambda = 0.4474$) efficiently removed the haze with more brilliant color and the highest value of UIQM = 5.786. Fig. 10 illustrates the image of Scene 4 from the AL-NG-OVD database associated with the recovery using different approaches. In contrast to other methods, our technique ($\mu_\lambda = 0.3964$) and the N-LID method unveiled the near foreground while preserving appropriate vagueness in the distant background. However, the foreground scene produced by the N-LID method was slightly greenish comparing to the proposed algorithm, which obtained the best evaluation measure value.

We show, in Fig. 11, the restoration results of Scene 5 image in the D-SD database. While the ICM, ERD, and IBLA methods partially removed the haze, the UDCP, ULSM, and N-LID schemes somewhat darkened the scene.

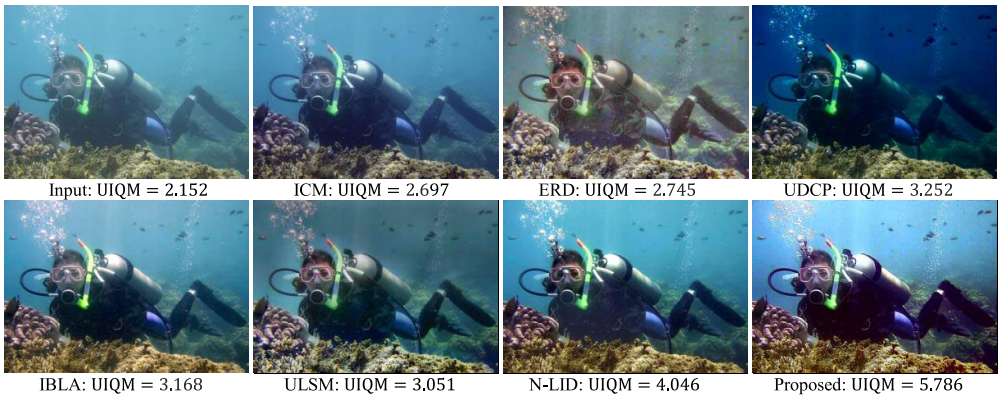

FIGURE 9. Visual comparison of restoration in Scene 3 image.

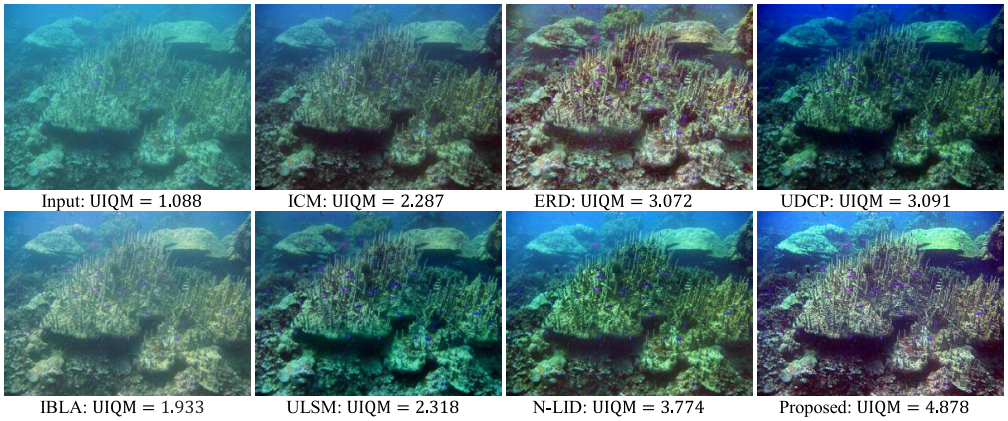

FIGURE 10. Visual comparison of restoration in Scene 4 image.

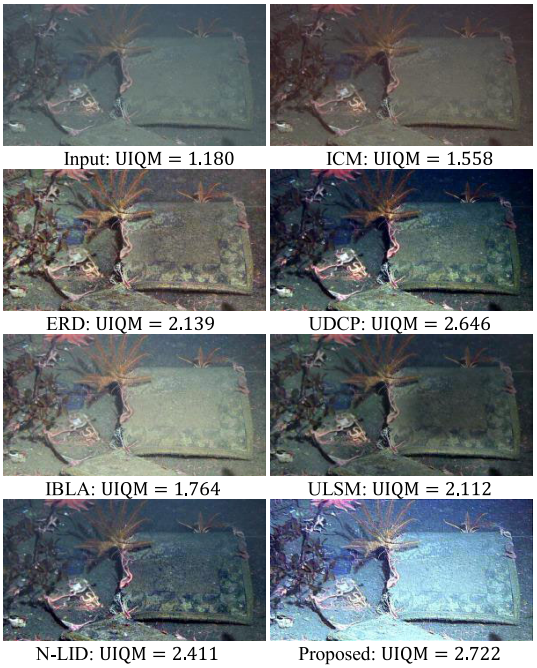

FIGURE 11. Visual comparison of restoration in Scene 5 image.

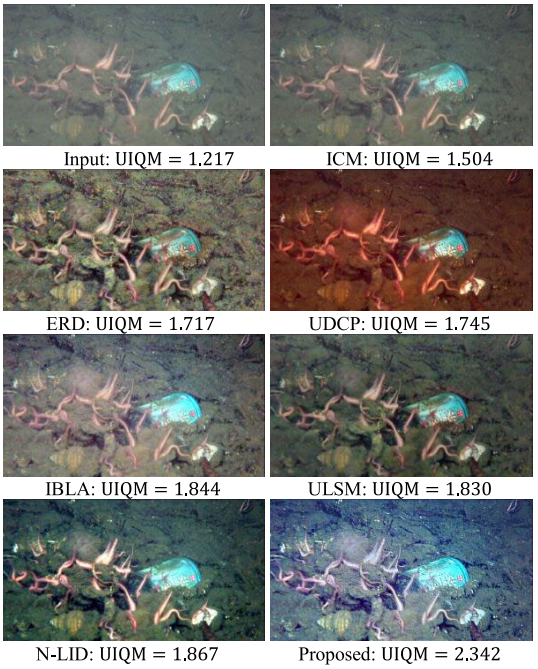

FIGURE 12. Visual comparison of restoration in Scene 6 image.

The restoration outcome of our proposed algorithm was more pleasant and visually brighter. Another example from the D-SD database is illustrated in Fig. 12. All methods lessened the haze with different degrees and tone changes. In contrast to other techniques, the restoration result of the UDCP method was reddish. Fig. 13 depicts the restoration

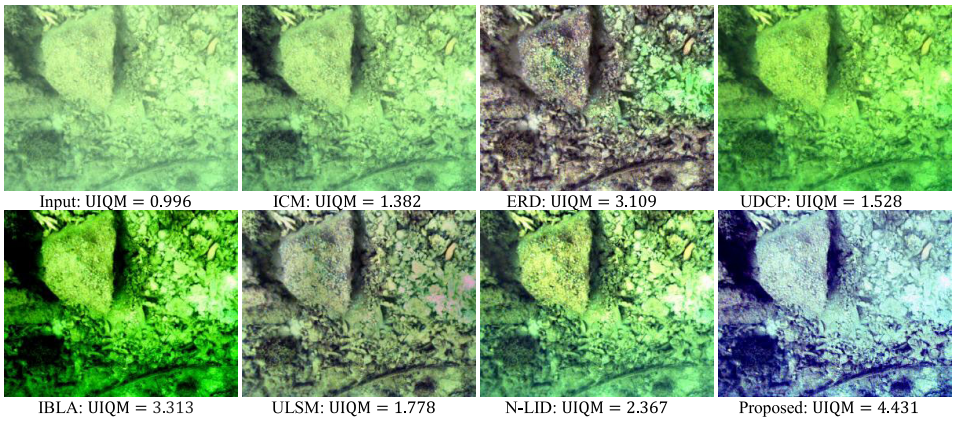

FIGURE 13. Visual comparison of restoration in Scene 7 image.

of a challenging underwater image in the HIMB database. The ICM, UDCP, IBLA, and N-LID methods were unable to discard the green tone. The restoration results of the ERD and ULSM methods exhibited some green distortion, whereas our algorithm more efficiently lessened the green tone with the best score of UIQM = 4.431. Finally, massive experiments were conducted on hundreds of underwater images in the three databases, whose restoration outcome using different methods is summarized in Table 2. It was noted that our proposed restoration algorithm produced the highest average evaluation scores in all databases.

Underwater image restoration with one single input image without further imaging information is highly challenging as demonstrated in the above experiments. The key to successful restoration relies upon accurate estimations of two important parameters: background light and transmission map. For model-based methods, assumptions with different degrees of simplification have been made in order to achieve practical implementations. For image-based approaches, techniques derived from various image processing theories and observations are typically exploited, without considering the image formation model. Since estimation errors are on a case-by-case basis, an adaptive mechanism to precisely correct errors is difficult to develop provided that only one underwater image is given. This study suggests an image fusion solution by integrating two different schemes that compensate each other to alleviate the influence of the unpredictable variation of vision properties in undersea environments, which improves the accuracy of estimation. As can be observed from the demonstration, the restoration by our algorithm strikes a good compromise between the model-based and image-based methods. Nevertheless, the integration of other methods for the background light and transmission map estimation through our proposed framework is worth investigating in the future.

V. CONCLUSION

In conclusion, this paper exclusively introduced a new underwater image restoration framework based on adaptive transmission fusion of two different approaches. By the incorporation of saliency maps, the resultant transmission map took advantage of both estimation strategies. A variety of simulated and underwater images with different scenarios of haze quality and color distortion were employed to evaluate the performance of the proposed framework. The restoration results were consistent with the philosophy of the proposed restoration schemes in that the foreground scene was efficiently corrected with high clarity and natural color while maintaining a certain level of vagueness in the background. Comparing to the state-of-the-art methods, our restoration results were generally more qualitatively pleasing and quantitatively convincing.

ACKNOWLEDGMENT

The author would like to thank Jun-Qi Li and Pin-Yi Kuan for executing the experiments and collecting experimental data.

REFERENCES

[1] S. G. Narasimhan, S. K. Nayar, B. Sun, and S. J. Koppal, "Structured light in scattering media," in *Proc. 10th IEEE Int. Conf. Comput. Vis. (ICCV)*, vol. 1, Oct. 2005, pp. 420–427.
[2] P. Bouguer, *Essai d'Optique Sur La Gradation de La Lumière [Optics Essay on the Attenuation of Light] (in French)*. Paris, France: Claude Jombert, 1729, pp. 16–22.
[3] R. Schettini and S. Corchs, "Underwater image processing: State of the art of restoration and image enhancement methods," *EURASIP J. Adv. Signal Process.*, no. 1, Apr. 2010, Art. no. 746052.
[4] D. Akkaynak, T. Treibitz, T. Shlesinger, Y. Loya, R. Tamir, and D. Iluz, "What is the space of attenuation coefficients in underwater computer vision?" in *Proc. IEEE Conf. Comput. Vis. Pattern Recognit. (CVPR)*, Jul. 2017, pp. 568–577.
[5] S. Q. Duntley, "Light in the sea," *J. Opt. Soc. Amer.*, vol. 53, no. 2, pp. 214–233, 1963.
[6] B. McGlamery, "A computer model for underwater camera systems," *Proc. SPIE*, vol. 208, pp. 221–231, Mar. 1980.
[7] J. Jaffe, "Computer modeling and the design of optimal underwater imaging systems," *IEEE J. Ocean. Eng.*, vol. 15, no. 2, pp. 101–111, Apr. 1990.
[8] Y. Y. Schechner and N. Karpel, "Clear underwater vision," in *Proc. IEEE Comput. Soc. Conf. Comput. Vis. Pattern Recognit. (CVPR)*, vol. 1, Jun./Jul. 2004, pp. I-536–I-543.
[9] E. Nascimento, M. Campos, and W. Barros, "Stereo based structure recovery of underwater scenes from automatically restored images," in *Proc. XXII Brazilian Symp. Comput. Graph. Image Process.*, Oct. 2009, pp. 330–337.
[10] K. Iqbal, R. A. Salam, A. Osman, and A. Z. Talib, "Underwater image enhancement using an integrated color model," *Int. J. Comput. Sci.*, vol. 34, no. 2, pp. 239–244, 2007.

[11] A. S. Abdul Ghani and N. A. Mat Isa, "Underwater image quality enhancement through integrated color model with Rayleigh distribution," *Appl. Soft Comput.*, vol. 27, pp. 219–230, Feb. 2015.
[12] H. Liu and L.-P. Chau, "Underwater image restoration based on contrast enhancement," in *Proc. IEEE Int. Conf. Digit. Signal Process. (DSP)*, Oct. 2016, pp. 584–588.
[13] C.-Y. Li, J.-C. Guo, R.-M. Cong, Y.-W. Pang, and B. Wang, "Underwater image enhancement by dehazing with minimum information loss and histogram distribution prior," *IEEE Trans. Image Process.*, vol. 25, no. 12, pp. 5664–5677, Dec. 2016.
[14] E. Trucco and A. Olmos-Antillon, "Self-tuning underwater image restoration," *IEEE J. Ocean. Eng.*, vol. 31, no. 2, pp. 511–519, Apr. 2006.
[15] J.-P. Tarel and N. Hautiere, "Fast visibility restoration from a single color or gray level image," in *Proc. IEEE 12th Int. Conf. Comput. Vis.*, Sep. 2009, pp. 2201–2208.
[16] S. Qiu, J. Yu, B. He, R. Nian, and A. Lendasse, "A novel adaptive restoration for underwater image quality degradation," in *Proc. OCEANS MTS/IEEE Washington*, Oct. 2015, pp. 1–5.
[17] X. Zhao, T. Jin, and S. Qu, "Deriving inherent optical properties from background color and underwater image enhancement," *Ocean Eng.*, vol. 94, pp. 163–172, Jan. 2015.
[18] X. Liu, G. Zhong, C. Liu, and J. Dong, "Underwater image colour constancy based on DSNMF," *IET Image Process.*, vol. 11, no. 1, pp. 38–43, Jan. 2017.
[19] Y. Cho and A. Kim, "Visibility enhancement for underwater visual SLAM based on underwater light scattering model," in *Proc. IEEE Int. Conf. Robot. Autom. (ICRA)*, May 2017, pp. 710–717.
[20] N. Wang, H. Zheng, and B. Zheng, "Underwater image restoration via maximum attenuation identification," *IEEE Access*, vol. 5, pp. 18941–18952, 2017.
[21] Y. Wang, H. Liu, and L.-P. Chau, "Single underwater image restoration using adaptive attenuation-curve prior," *IEEE Trans. Circuits Syst. I, Reg. Papers*, vol. 65, no. 3, pp. 992–1002, Mar. 2018.
[22] D. Berman, T. Treibitz, and S. Avidan, "Non-local image dehazing," in *Proc. IEEE Conf. Comput. Vis. Pattern Recognit. (CVPR)*, Jun. 2016, pp. 1674–1682.
[23] X. Deng, H. Wang, and X. Liu, "Underwater image enhancement based on removing light source color and dehazing," *IEEE Access*, vol. 7, pp. 114297–114309, 2019.
[24] J. Wang, H. Wang, G. Gao, H. Lu, and Z. Zhang, "Single underwater image enhancement based on L_P-norm decomposition," *IEEE Access*, vol. 7, pp. 145199–145213, 2019.
[25] K. Cao, Y.-T. Peng, and P. C. Cosman, "Underwater image restoration using deep networks to estimate background light and scene depth," in *Proc. IEEE Southwest Symp. Image Anal. Interpretation (SSIAI)*, Apr. 2018, pp. 1–4.
[26] P. Liu, G. Wang, H. Qi, C. Zhang, H. Zheng, and Z. Yu, "Underwater image enhancement with a deep residual framework," *IEEE Access*, vol. 7, pp. 94614–94629, 2019.
[27] K. He, J. Sun, and X. Tang, "Single image haze removal using dark channel prior," *IEEE Trans. Pattern Anal. Mach. Intell.*, vol. 33, no. 12, pp. 2341–2353, Dec. 2011.
[28] Z. Li, J. Zheng, W. Yao, and Z. Zhu, "Single image haze removal via a simplified dark channel," in *Proc. IEEE Int. Conf. Acoust., Speech Signal Process. (ICASSP)*, Apr. 2015, pp. 1608–1612.
[29] K. B. Gibson and T. Q. Nguyen, "On the effectiveness of the Dark Channel Prior for single image dehazing by approximating with minimum volume ellipsoids," in *Proc. IEEE Int. Conf. Acoust., Speech Signal Process. (ICASSP)*, May 2011, pp. 1253–1256.
[30] T. Han and Y. Wan, "A fast dark channel prior-based depth map approximation method for dehazing single images," in *Proc. IEEE 3rd Int. Conf. Inf. Sci. Technol. (ICIST)*, Mar. 2013, pp. 1355–1359.
[31] J. Y. Chiang and Y.-C. Chen, "Underwater image enhancement by wavelength compensation and dehazing," *IEEE Trans. Image Process.*, vol. 21, no. 4, pp. 1756–1769, Apr. 2012.
[32] J.-K. Guo, C.-C. Sung, and H.-H. Chang, "Improving visibility and fidelity of underwater images using an adaptive restoration algorithm," in *Proc. OCEANS TAIPEI*, Apr. 2014, pp. 1–6.
[33] A. Galdran, D. Pardo, A. Picón, and A. Alvarez-Gila, "Automatic red-channel underwater image restoration," *J. Vis. Commun. Image Represent.*, vol. 26, pp. 132–145, Jan. 2015.
[34] P. L. Drews, E. R. Nascimento, S. S. Botelho, and M. F. M. Campos, "Underwater depth estimation and image restoration based on single images," *IEEE Comput. Grap. Appl.*, vol. 36, no. 2, pp. 24–35, Mar. 2016.
[35] S. Borkar and S. V. Bonde, "Underwater image restoration using single color channel prior," in *Proc. Int. Conf. Signal Inf. Process. (IConSIP)*, Oct. 2016, pp. 1–4.
[36] Z. Li and J. Zheng, "Edge-preserving decomposition-based single image haze removal," *IEEE Trans. Image Process.*, vol. 24, no. 12, pp. 5432–5441, Dec. 2015.
[37] W. Hou, D. J. Gray, A. D. Weidemann, G. R. Fournier, and J. L. Forand, "Automated underwater image restoration and retrieval of related optical properties," in *Proc. IEEE Int. Geosci. Remote Sens. Symp.*, Jul. 2007, pp. 1889–1892.
[38] Y. Tian and S. G. Narasimhan, "Seeing through water: Image restoration using model-based tracking," in *Proc. IEEE 12th Int. Conf. Comput. Vis.*, Sep. 2009, pp. 2303–2310.
[39] C. Li, J. Guo, S. Chen, Y. Tang, Y. Pang, and J. Wang, "Underwater image restoration based on minimum information loss principle and optical properties of underwater imaging," in *Proc. IEEE Int. Conf. Image Process. (ICIP)*, Sep. 2016, pp. 1993–1997.
[40] Y.-T. Peng and P. C. Cosman, "Underwater image restoration based on image blurriness and light absorption," *IEEE Trans. Image Process.*, vol. 26, no. 4, pp. 1579–1594, Apr. 2017.
[41] K. He, J. Sun, and X. Tang, "Guided image filtering," *IEEE Trans. Pattern Anal. Mach. Intell.*, vol. 35, no. 6, pp. 1397–1409, Jun. 2013.
[42] H.-H. Chang, C.-Y. Cheng, and C.-C. Sung, "Single underwater image restoration based on depth estimation and transmission compensation," *IEEE J. Ocean. Eng.*, vol. 44, no. 4, pp. 1130–1149, Oct. 2019.
[43] H. B. Mitchell, *Image Fusion Theories, Techniques and Applications*. Berlin, Germany: Springer-Verlag, 2010.
[44] A. Ardeshir Goshtasby and S. Nikolov, "Image fusion: Advances in the state of the art," *Inf. Fusion*, vol. 8, no. 2, pp. 114–118, Apr. 2007.
[45] S. Chaudhuri, *Hyperspectral Image Fusion by Subhasis Chaudhuri*, K. Kotwal, Ed. New York, NY, USA: Springer, 2013.
[46] O. Rockinger and T. Fechner, *Pixel-Level Image Fusion: The Case of Image Sequences* (Aerospace/Defense Sensing and Controls). Bellingham, WA, USA: SPIE, 1998.
[47] C. Tomasi and R. Manduchi, "Bilateral filtering for gray and color images," in *Proc. 6th Int. Conf. Comput. Vis.*, Nov. 2002, pp. 839–846.
[48] C. O. Ancuti and C. Ancuti, "Single image dehazing by multi-scale fusion," *IEEE Trans. Image Process.*, vol. 22, no. 8, pp. 3271–3282, Aug. 2013.
[49] G. R. Ayers and J. C. Dainty, "Iterative blind deconvolution method and its applications," *Opt. Lett.*, vol. 13, no. 7, p. 547, Jul. 1988.
[50] K. Panetta, C. Gao, and S. Agaian, "Human-visual-system-inspired underwater image quality measures," *IEEE J. Ocean. Eng.*, vol. 41, no. 3, pp. 541–551, Jul. 2016.
[51] *Aqua Life Images*. Accessed: Jan. 2016. [Online]. Available: http://www.aqualifeimages.com/default.aspx
[52] *National Geographic*. Accessed: May 2017. [Online]. Available: http://www.nationalgeographic.com/
[53] *Ocean View Diving*. Accessed: Mar. 2018. [Online]. Available: http://www.oceanviewdive.com/gallery-2/
[54] *Deep-sea Debris Database*. Accessed: Dec. 2019. [Online]. Available: http://www.godac.jamstec.go.jp/catalog/dsdebris/e/index.html
[55] K. A. Skinner, J. Zhang, E. A. Olson, and M. Johnson-Roberson, "UWStereoNet: Unsupervised learning for depth estimation and color correction of underwater stereo imagery," in *Proc. Int. Conf. Robot. Autom. (ICRA)*, May 2019, pp. 7947–7954.

HERNG-HUA CHANG (Member, IEEE) received the B.S. degree in mechanical engineering from National Taiwan University, Taipei, Taiwan, in 1996, the M.S. degree in biomedical engineering from National Yang-Ming University, Taiwan, in 1998, and the Ph.D. degree in biomedical engineering from the University of California at Los Angeles (UCLA), in 2006.

He was formerly a Postdoctoral Scholar with the Laboratory of Neuro Imaging (LONI) and a member of the Center for Computational Biology (CCB), UCLA. He joined National Taiwan University as an Assistant Professor, in 2010. He is currently an Associate Professor with the Department of Engineering Science and Ocean Engineering, National Taiwan University. His research interests include variational methods for image restoration, registration and segmentation, computational biology and radiology, artificial intelligence techniques for image processing, pattern analysis and computer graphics, and medical informatics for healthcare applications.